Pursuant to the DOE Public Access Plan, this document represents the authors' peer-reviewed, accepted manuscript. The published version of the article is available from the relevant publisher.

ACS APPLIED MATERIALS **XINTERFACES**

Research Article www.acsami.org

A Multi-modal Approach to Understanding Degradation of Organic **Photovoltaic Materials**

Michael A. Anderson, Bryon W. Larson,* and Erin L. Ratcliff*



Cite This: https://doi.org/10.1021/acsami.1c12321



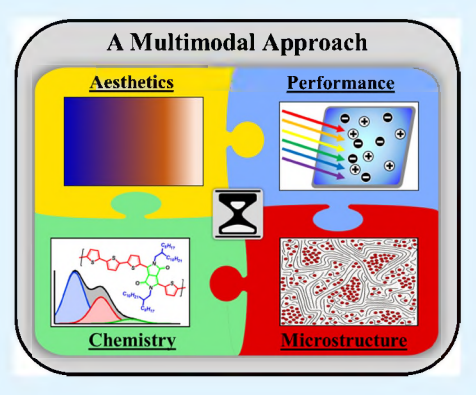
ACCESS I

Metrics & More

Article Recommendations

Supporting Information

ABSTRACT: State-of-the-art organic photovoltaic (OPV) materials are composed of complex, chemically diverse polymeric and molecular structures that form highly intricate solid-state interactions, collectively yielding exceptional tunability in performance and aesthetics. These properties are especially attractive for semitransparent power-generating windows or shades in living environments, greenhouses, or other architectural integrations. However, before such a future is realized, a broader and deeper understanding of property stability must be acquired. Stability during operating and environmental conditions is critical, namely, material color steadfastness, optoelectronic performance retention, morphological rigidity, and chemical robustness. To date, no single investigation encompasses all four distinct, yet interconnected, metrics. Here, we present a multimodal strategy that captures a dynamic and interconnected evolution of each property during the course of an accelerated photobleaching experiment. We demonstrate this approach across relevant



length scales (from molecular to visual macroscale) using X-ray photoelectron spectroscopy, grazing-incidence X-ray scattering, microwave conductivity, and time-dependent photobleaching spectroscopies for two high-performance semitransparent OPV blends—PDPP4T:PC60BM and PDPP4T:IEICO-4F, with comparisons to the stabilities of the individual components. We present direct evidence that specific molecular acceptor (fullerene vs nonfullerene) designs and the resulting donor-acceptor interactions lead to distinctly different mechanistic routes that ultimately arrive at what is termed "OPV degradation." We directly observe a chemical oxidation of the cyano endcaps of the IEICO-4F that coincides with a morphological change and large loss in photoconductivity while the fullerene acceptor-containing blend demonstrates a significantly greater fraction of oxygen uptake but retains 55% of the photoconductivity. This experimental roadmap provides meaningful guidance for future high-throughput, multimodal studies, benchmarking the sensitivity of the different analytical techniques for assessing stability in printable active layers, independent of complete device architectures.

KEYWORDS: organic photovoltaics, degradation, performance, aesthetic, morphological stability

1. INTRODUCTION

Organic photovoltaics (OPV) have advantages of being lightweight, flexible, and offer synthetic control of properties such as color and transmissivity. Manufacturing scalability, low energy payback times, and excellent color-tunability attributes have made these devices extremely attractive for portable and point-of-use solar applications, such as solar tents, windows, and PV-integrated greenhouses.²⁻⁵ Efficiencies continue to improve, with certified single junctions approaching 18% power conversion efficiency (PCE) to date, capitalizing on five decades of multidisciplinary research into structure-property design rules for OPV materials. Of particular note is the historic development of nonfullerene acceptors (NFAs), which provide additional degrees of freedom in chemical tunability compared to fullerene predecessors.

The final frontier for OPV commercialization is stability, particularly as NFAs have introduced new complications toward its understanding.8 Generally, OPV stability is defined as the retention (or loss) of PCE over time. However, comparisons between studies—even ones involving the same active layer—are challenging due to the diversity in device architectures (active layer compositions, contact selections, encapsulation strategies, environmental, and stress-testing conditions) and the undetermined effects of film processing and additives. Postmortem quantitative analysis of buried interfaces and the ambiguity in deciphering mechanistic insight from a current-voltage curve continue to be major hurdles. Alternatively, chemical degradation studies on the components of the active layer alone can provide mechanistic context, such as photocatalyzed oxygen addition to molecular frameworks.

Received: June 30, 2021



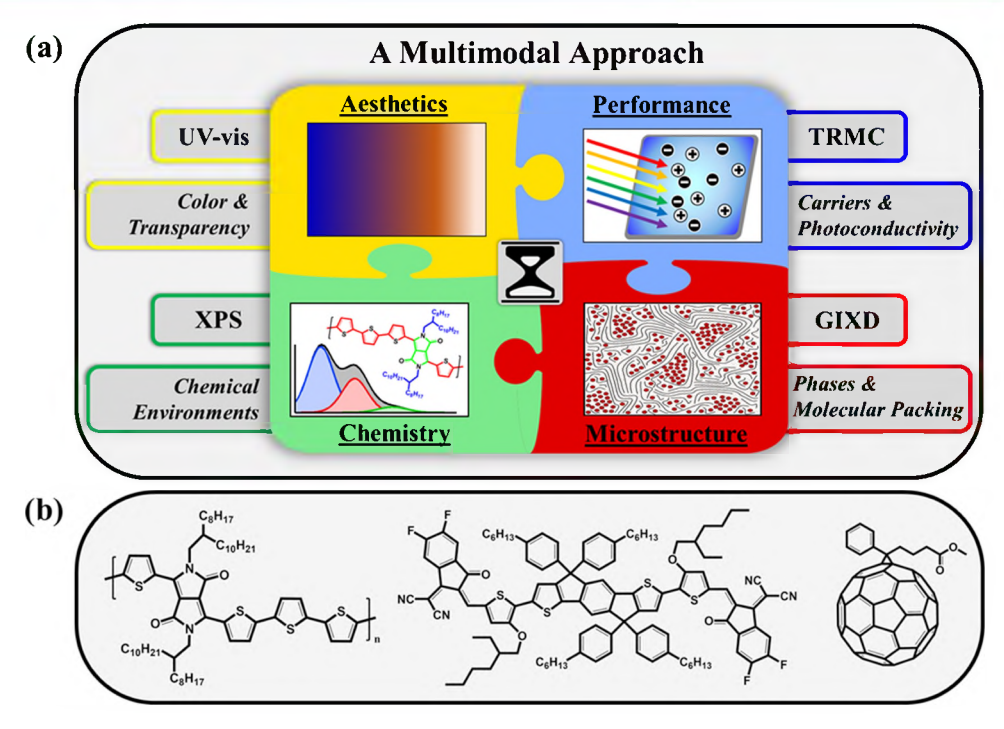


Figure 1. (a) Multimodal approach to OPV active layer degradation and applied techniques including UV–visible absorption, time-resolved microwave conductivity (TRMC), X-ray photoelectron spectroscopy (XPS), and grazing-incidence X-ray diffraction (GIXD). (b) Chemical structures of PDPP4T, IEICO-4F, and $PC_{60}BM$ (left to right).

Yet, these quantifiable investigations struggle to provide device context, often ignoring the role of chemically induced traps to reduction in efficiencies and/or underlying changes in microstructure. Herein, we bridge the disparate device and chemistry approaches and focus on the complex, interconnected factors of stability. We define stability as a deviation to reference in four specific criteria: intrinsic molecular chemistry (both inter- and intramolecular chemical/thermal/photostability as alterations to chemical bonds), blend morphology stability (the dynamic physical arrangement of the mixed semiconductors), retention of optoelectronic processes (exciton dissociation, charge mobility, carrier lifetime), and color steadfastness—all of which are interrelated and translate to and have an impact on performance, application, and operating lifetime.

Figure 1a shows the schematic overview of applying a multimodal approach that disentangles all four of the previously believed inextricable property—performance relationships (material color steadfastness, optoelectronic performance retention, chemical robustness, and morphological rigidity) for a set of neat and blended OPV heterojunctions during accelerated photoabsorption stress testing.

Our measurement toolbox includes: (i) accelerated degradation as both a function of photon flux and time in the ambient environment, coupled with in situ absorptance measurements (UV-vis) to track color changes; (ii) time-resolved microwave conductivity (TRMC) to assess changes in photoconductivity and the dynamic excited state processes involved in photoinduced charge generation and transport; (iii) X-ray photoelectron spectroscopy (XPS) to capture any potential intrinsic chemistries at the inter-and intramolecular levels; and (iv) grazing-incidence X-ray diffraction (GIXD), or scattering, to monitor intermolecular packing and blend phase changes. This information must be known to anticipate how new structures and blend compositions may fare during

operation over time and collectively examining these data enable us to bridge the gap between device and chemistry degradation studies.

Ambient photobleaching and in situ absorptance measurements (i) are accomplished via the automated in situ photobleaching spectrometer (AIPS), which has been previously described. In brief, the AIPS affords simultaneous photobleaching of multiple films in ambient with automated transmission and reflection measurements taken periodically. Where the AIPS affords a real-time in situ monitoring of color changes, the other tools in our multimodal capability are discrete, necessitating samples at specific degradation setpoints for characterization. The optoelectronic performance (ii) of the blends was quantified via TRMC, which requires samples to be placed in the path of both a pulsed laser and a microwave, but allows for photoconductivity measurements of films on bare substrates, consistent with the other experimental methods. TRMC is a laser-pump microwave-probe technique that monitors the time-resolved evolution of photoinduced carrier generation and recombination dynamics in stand-alone films, i.e., a film that is deposited on bare quartz with no electrical contacts or extraction layers present. For this study, we rely on TRMC data to complement and inform a deeper understanding of how the optoelectronic properties of each blend film were affected by the accelerated photobleaching experiment with respect to the additional changes that were characterized using our multimodal approach. The chemical environments (iii) of neat and blended films are investigated using XPS, necessitating the collection of photoelectrons in ultrahigh vacuum. Chemical analysis of the materials demonstrates the key spectroscopic signatures of each molecular component in the core levels as well as enables some insight into bond breakage and/or formation in the materials. Finally, morphological characterizations (iv) are made by combining the results of two GIXD techniques that

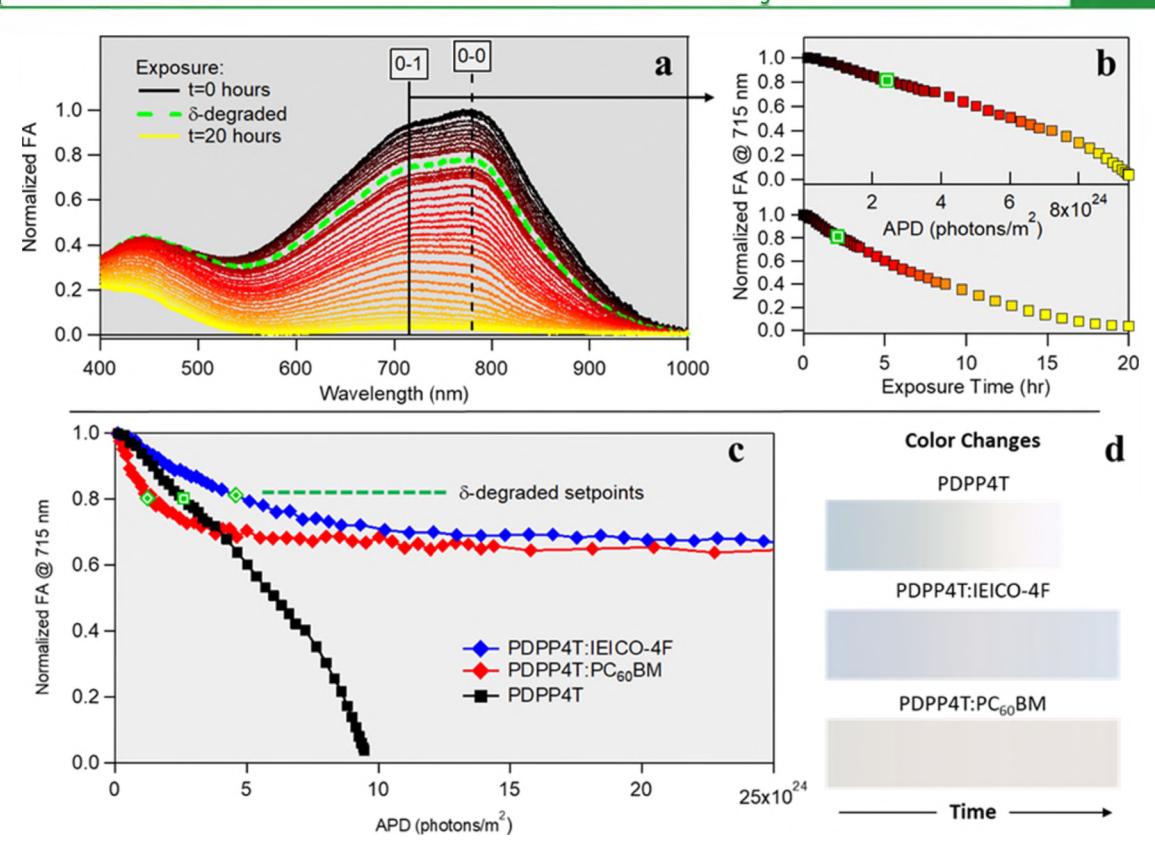


Figure 2. (a) FA vs wavelength progression for neat PDPP4T over 20 h of ambient light exposure, (b) PDPP4T FA vs APD and exposure time at the 0–1 transition peak wavelength (715 nm), (c) FA vs APD of PDPP4T and blends at 715 nm, and (d) color changes throughout exposure.

require synchrotron radiation due to the low scattering profiles of organics. The techniques are grazing-incidence wide-angle X-ray scattering (GIWAXS), informing on the intermolecular spacings of semicrystalline regions in the neat and blended films, and grazing-incidence small-angle X-ray scattering (GISAXS), which gives the average size of domains in the blended heterojunctions. Combining these methods, we strategically demonstrate the power of such a multimodal approach using prototypical materials that have potential in semitransparent OPV applications.

First, we focus on a low-band-gap polymer poly[2,5-bis(2octyldodecyl)pyrrolo[3,4-c]pyrrole-1,4(2H,5H)-dione-3,6diyl)-alt-(2,2';5',2";5",2"'-quaterthiophen-5,5"'-diyl)] (PDPP4T), shown in Figure 1b. This donor polymer was chosen as it is commercially available, has demonstrated a high hole mobility, 12 represents a modern push-pull polymer design, and has redox levels that favor high charge separation probabilities with our common acceptors (PC60BM and IEICO-4F), all of which are expected from high-efficiency OPV systems. The highest molecular orbital of \sim 5.2 eV should result in an intrinsically stable ground state to oxygen reactions, while we hypothesize that the 4.0 eV LUMO could participate in photooxidation of the excited state.¹³ Additionally, we note the unique reporter sulfur atoms on the push unit relative to the nitrogen atoms on the pull unit, enabling localized information on chemical degradation via

To give broader context to both historical and emerging blended architectures, PDPP4T was paired with $PC_{60}BM$ and IEICO-4F. These two heterojunctions represent two viable options for semitransparent device applications covering both approaches to accomplish the same: blending with an acceptor

that absorbs more UV ($PC_{60}BM$) vs one that absorbs more NIR (IEICO-4F). In either case, power conversion efficiencies of 5.62% for PDPP4T with a fullerene ($PC_{70}BM$) and 9.13% for IEICO-4F blends^{14,15} have been published, and we note that devices have already been engineered with nearly complete visual transparency while retaining reasonable efficiencies as demonstrated by Lee et al. for PDPP4T:IEI-CO-4F (5.7%). We demonstrate that our approach uniquely captures the fullerene vs NFA interactions within the host polymer, desirable aesthetics but different absorption profiles, and significantly different innate chemical reactivities and morphological packing tendencies.

While a number of possible mechanisms exist in degradation of organic semiconductors (radical propagation, oxygen addition, residual catalyst effects), ^{13,16} in the application of our multimodal approach, we quantify degradation against the number of photons absorbed by the sample, rather than focusing on time passed, to account for the differences in absorption profiles and intensities between samples. This allows us to both quantify the chemical degradation hypothesis, where light is considered a reactant, and give context to thermally assisted diffusion leading to microstructure instabilities. A number of demonstrations exist whereby the donor is stabilized by pairing with an acceptor, ^{9,17–19} although we have also observed that this is not always the case. ²⁰

In the following sections, we describe a path to understand degradation especially in this category of OPV materials (i.e., where aesthetics matter as much as if not more than performance), yet the multimodal approach is not limited to semitransparent OPV. Our findings and multimodal approach lay foundational groundwork for use-inspired and targeted

Research Article

investigations of OPV material stability that in turn enables a more informed decision-making process when selecting or designing OPVs for applications that require robust long-term performance and aesthetics.

2. RESULTS AND DISCUSSION

2.1. Aesthetics—Photobleaching via AIPS. We selected to degrade the organic semiconductor materials in ambient conditions using the AIPS system as an accelerated degradation protocol. Monitoring the photobleaching kinetics is a high-level approach to qualitatively evaluate changes in optical bandgap and observe indications of chemical and/or microstructural instability as optical transitions in the donor and acceptors evolve during light soaking. In general, OPV materials stored in inert, dark conditions predominantly exhibit minimal color change, whereas materials exposed to continuous photon dosing (light soaking) in ambient display rapid lightening and/or decolorization in a matter of hours to days. These generalizations have been used to argue in support of a photo-assisted decomposition mechanism involving oxygen, predominantly assumed to be interacting with the excited state of the donor material.¹³ We therefore monitor the absorption profiles and intensities of the neat and blended films while exposed to continuous illumination in ambient.

Figure 2a shows the fractional absorptance (FA) changes of neat PDPP4T over 400–1000 nm as a function of time. The primary absorption features of PDPP4T were completely lost after 20 h of exposure, illustrating the unstable nature of the neat donor materials. Comparative changes in FA for the pure acceptor films (PC $_{60}$ BM and IEICO-4F) as well as the blends are given in the Supporting Information (Figures S1–S5).

In Figure 2a, as-cast PDPP4T (t = 0, APD = 0) has a maximum at 780 nm (1.59 eV), attributed to the 0-0 vibronic transition and a slightly higher-energy/lower-wavelength shoulder at 715 nm (1.73 eV) associated with the 0-1 transition. There is also a high-energy transition at ~440 nm (~2.8 eV) that is due to intrinsic DPP (pull unit) chromophore absorption, to be differentiated from the lowerenergy 0-1 transition of the full repeat unit. 21-24 The 0-0 transition, while theoretically forbidden, occurs due to the intricacies of intermolecular interactions, disorder, and relaxations that occur with $\pi-\pi$ stacking of polymer chains. We note that no $\pi-\pi$ stacking was detectable in GIWAXS for the polymer, either as-cast or partially degraded. However, we observe an initial 0-0:0-1 ratio of 1.07. With photobleaching, disruption of the 0-0 transition advances more rapidly than that of the 0-1 transition and eventually results in a 0-0:0-1 less than 1.

We focus herein on the 0–1 transition of PDPP4T at 715 nm to elucidate the impact of photodegradation on the intrinsic absorption mechanism of the donor and to allow for direct comparison to polymer color change when incorporated in the blended heterojunctions. Specifically, PC₆₀BM absorption is negligible at 715 nm and the absorption feature of IEICO-4F is stable in this region (Figures S2 and S3). Figure 2b shows the FA of PDPP4T at 715 nm vs time and APD for comparison, where the APD was calculated using the spectral output from the illumination source and the transient FA spectra. For studies focusing on light as a reactant, APD is a better choice, as it allows for comparison between materials that absorb differently (both spectrally and intensity). More explicitly, materials photodegraded for the same amount of time may have absorbed drastically different photon doses, and

thus would have different probabilities of degradation if light is a reactant.

Figure 2c shows the comparative FA of the polymer 0-1 transition wavelength (715 nm) in 1:1 blend ratios with either acceptor. For context, the color changes throughout exposure time as calculated from absorptance data are given in Figure 2d. In both cases, we observe that the acceptors suppress photodegradation of PDPP4T, hypothesized to be due to donor—acceptor charge transfer competing with radicalinitiated photooxidation of the donor excited state, with absorptance loss of neat PDPP4T being significantly reduced in blends. Both acceptors stabilize the 0-1 transition of the donor to the same degree past 10×10^{24} photons m⁻² and both materials in the blends were still contributing to the color and absorption even after 120 h of exposure (Figures S4 and S5).

We highlight two phenomena in Figure 2c: differences in the initial rate of PDPP4T 0-1 peak loss, a reduction for the IEICO-4F blend and increase for the PC₆₀BM blend relative to neat PDPP4T, and eventual stabilization in both blends after ~30% FA loss. This photodosing window suggests that in both blends, a certain favorable kinetic pathway is retained which favors photobleaching. One rationale is to attribute the lost chromophores to a near-pure amorphous phase of the donor. Photogenerated radicals in this phase have no proximal acceptor to be scavenged by and charge transfer to a different phase is less efficient due to the lack of crystallinity. The rate of PDPP4T FA loss in the IEICO-4F blend exhibited a clear initial reduction in slope compared to neat PDPP4T and eventual stabilization to \sim 70% FA past 10 \times 10²⁴ APD where neat PDPP4T had lost all absorbing capability. Interestingly, the initial $(0-2 \times 10^{24} \text{ APD})$ rate of FA loss for PDPP4T in the PC60BM blend was greater than that of neat PDPP4T, but then slowed and as in the case of the IEICO-4F blend, became stable around 70% FA past 10×10^{24} APD. We ascribe these differences to the convolution of two key attributes of the blends: relative D:A mixing and participation of the A in absorption of the photobleaching spectrum.

Fullerene derivatives with relatively low electron affinities have been demonstrated to catalyze photooxidation through a mechanism; Hoke et al describe this as "both the polymer and fullerene donate photogenerated electrons to diatomic oxygen to form the superoxide radical anion which degrades the polymer". 18 It is possible this mechanism is occurring here but we readily note in the study by Hoke et al, PC₆₀BM had the highest EA of fullerenes considered and was demonstrated to stabilize degradation. Alternatively, as discussed in the microstructure section below, the as-cast PC₆₀BM blend had domains of pure acceptor, indicating some degree of phase segregation, whereas the IEICO-4F blend was highly mixed. This implies there is a greater fraction of the photooxidationsusceptible, near-pure, amorphous PDPP4T in the fullerene blend to start. We observe that the acceptor domain sizes for both blends were equivalent by the ∂ -degraded setpoints, which explains why the two blends' FA curves converge to ~70% FA. In tandem, the IEICO-4F absorption spectrum overlaps with that of PDPP4T, implying that some fraction of the APD resulted in radicals generated in the relatively stable acceptor and not the donor, effectively removing that fraction of light as a reactant for donor photooxidation. In contrast, PC₆₀BM only absorbs in the near UV and has marginal overlap with PDPP4T. Since the photobleaching spectrum is predominately visible to near-IR (Figure S6), nearly all of

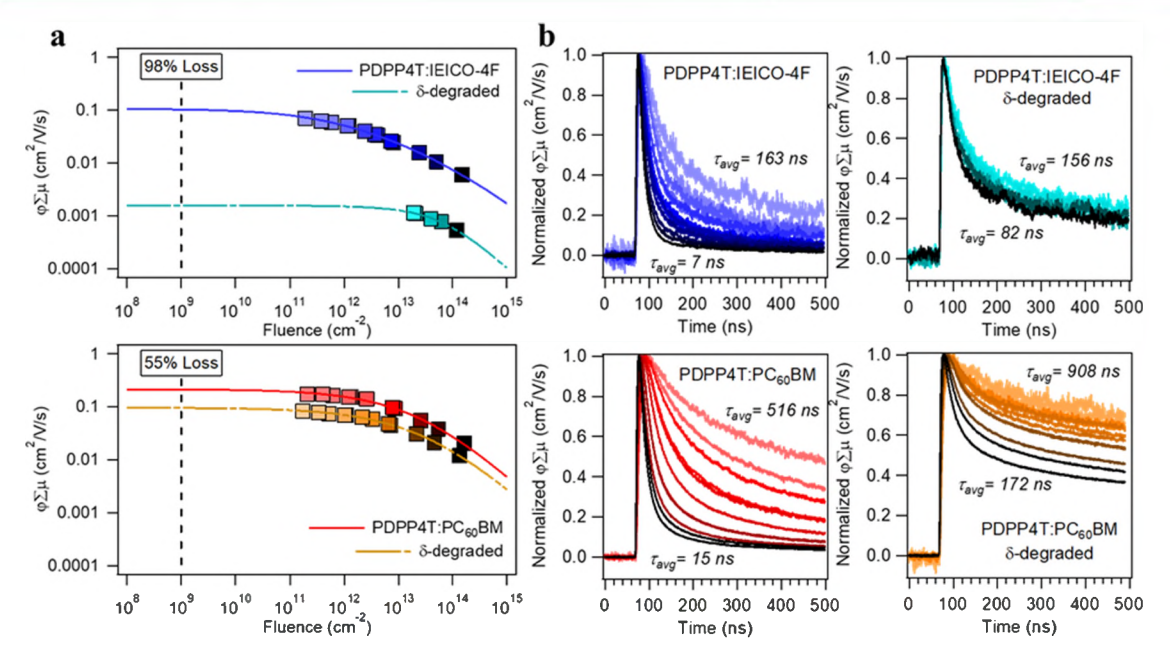


Figure 3. (a) Photoconductivity as end-of-pulse $\phi \sum \mu$ vs fluence as determined by TRMC for the as-cast and δ-degraded blends. (b) Normalized $\phi \sum \mu$ transients for different fluences color-coded in panel a for the as-cast and δ-degraded blends.

the APD for that blend originates in the donor, increasing the probability of the degrading reaction pathway.

As previously mentioned, while the AIPS affords a real-time in situ monitoring of absorption profiles, our other techniques require specific degradation setpoints to investigate the remaining stability criteria. Thus, we identified δ -degraded setpoints (green) in Figure 2, which correspond to 20% loss of peak absorption, independent of exposure time or accumulated photon dose (APD), to further elucidate the onset in photodegradation. Specifically, we hypothesize that the observed 20% FA loss corresponds to a detectable level of chemistry and/or microstructure, but as the films are not completely photobleached, heterojunctions would still demonstrate measurable photoconductivity and carrier lifetimes. Each of these effects is described in more detail below for neat and blends, where appropriate.

2.2. Performance—Photoconductivity via TRMC. Time-resolved microwave conductivity (TRMC) measurements were performed to assess the intrinsic photoconductivity of the films before and after photobleaching. Notably, the TRMC figures of merit (yield-mobility product, $\varphi \sum \mu$, and average photoconductivity lifetime, $\tau_{\rm avg}$) intrinsically qualify the material from a photovoltaic perspective, and have been shown to correlate to power conversion efficiency in optimally fabricated OPV devices. Therefore, TRMC is valuable for characterizing changes in optoelectronic performance, enabling us to distinguish intrinsic degradation within the active layer without the need for fabricating a complex device stack around it. Figure 3 shows the intensity dependence of $\varphi \sum \mu$ (a) and the normalized photoconductivity transients (b) from which $\varphi \sum \mu$ and tau are determined for the PDPP4T:IEICO-4F and PDPP4T:PC₆₀BM blends.

For the as-cast blends, the $\varphi \sum \mu_{\rm sat}$ values (Figure 3a) are in the range of 0.1–0.2 cm²/Vs, which is not surprising taking into account high hole mobilities observed in DPP-based polymers. ¹² After photobleaching to the δ -degraded positions, the blends exhibit strikingly different losses in $\varphi \sum \mu_{\rm sat}$; a 55% loss is observed for the fullerene blend, whereas a 98% loss is

observed for the nonfullerene blend, a trend consistent with reported efficiency losses of FA vs NFA blended devices. We note that even though the δ -degraded condition for the IEICO-4F blend has overlapping absorption between the donor and acceptor, the fraction of light absorbed for each sample at each condition is accounted for in the F_A term of the TRMC analysis. In Figure 3a, the lines are fits of the data, 33,34 using eq. 1

$$\varphi \sum \mu_{\text{sat}} = \frac{A}{1 + \sqrt{BI_0 FA} + CI_0 FA} \tag{1}$$

where A, B, and C are empirical fitting parameters used to interpolate to a low-fluence saturated value ($\varphi \sum \mu_{\rm sat}$) corresponding to 1 sun intensity (ca. 10^9 photons cm⁻²). At high excitation fluences, the data depicts a square root dependence, primarily ascribed to higher-order recombination losses within and immediately following the 5 ns laser pulse. In principle, the most highly intermixed regions of the film would be most susceptible to higher-order recombination at high intensities since the spatial proximities (interaction probability) of excitons and free carriers would also be the highest in these regions of the film. Such a situation would be corroborated by a dramatic spread in photoconductivity lifetime between the lowest and highest fluence data, which is indeed observed.

Figure 3b shows normalized photoconductivity transients for the blends as-cast and at δ -degraded conditions, recorded over 3 orders of magnitude of 800 nm excitation intensity, colored to correspond directly to the $\varphi \sum \mu$ vs fluence plot in Figure 3a. Each as-cast blend exhibits a large spread in average lifetime from the highest to lowest fluence transient (7–163 ns for the IEICO-4F blend and 15–516 ns for the PC₆₀BM blend), which is consistent with each film initially having some regions composed of finely mixed donor and acceptor. Lifetime values are extracted using biexponential fits of the data as shown in Figure S7 with the average lifetime determined by the equation

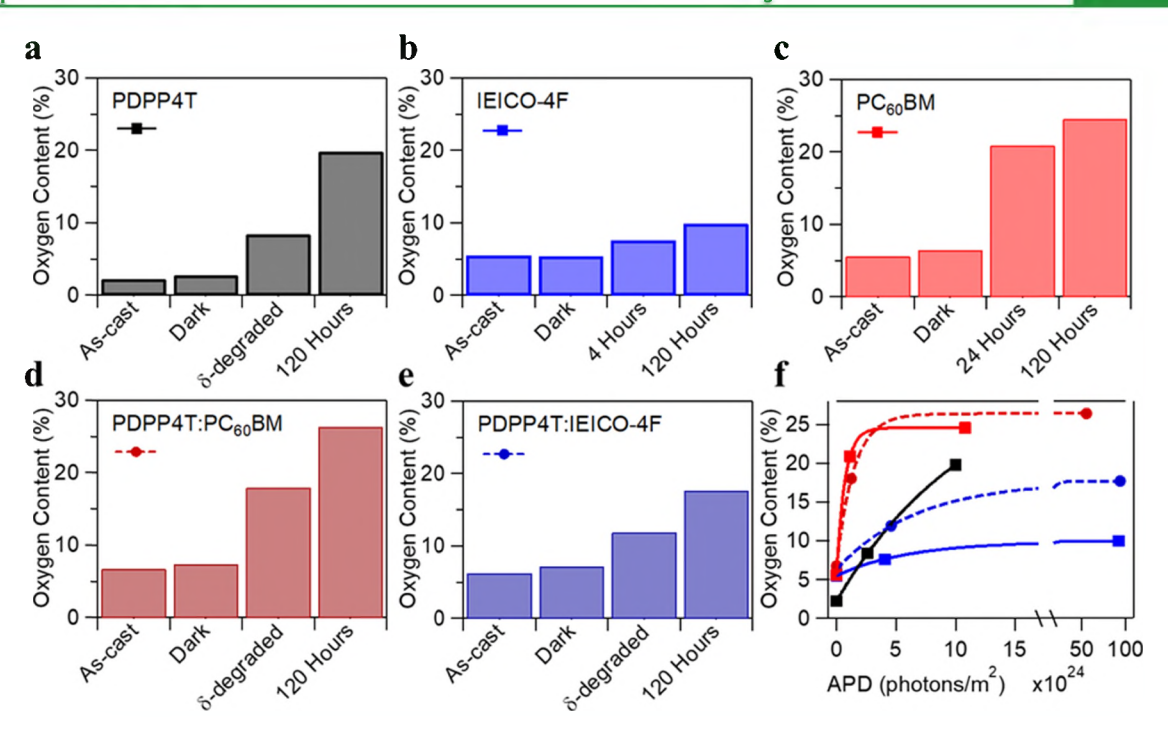


Figure 4. (a–e) Percent atomic concentration of oxygen for films as-cast, left in the dark in ambient for 120 h, partial and δ -degraded, and photodegraded in ambient for 120 h. (f) Fits of percent atomic concentration of oxygen vs APD throughout 120 h of photodegradation.

$$\tau_{\text{avg}} = \frac{A_{\text{s}}\tau_{\text{s}} + A_{\text{l}}\tau_{\text{l}}}{A_{\text{s}} + A_{\text{l}}} \tag{2}$$

where τ_s and τ_l are the short- and long-time constants, respectively, and A_s and A_l are their weighting coefficients.

The pre- and post-degraded transients also reveal significant changes to the lifetimes in each blend; in both cases, the loss of photoconductivity signal at earliest times (τ_s) is the most pronounced change and is most significant for the highest fluences measured. For example, comparing between the ascast the δ -degraded transients at the highest excitation intensity, the fractional contribution of τ_s to the average lifetime shrinks from 98 to 83% for the IEICO-4F blend and from 94 to 78% in the PC $_{60}$ BM blend. Meanwhile, the $au_{\rm s}$ value itself increases from 3 to 9 ns and 5 to 8 ns for the IEICO-4F and PC60BM blends, respectively. Clearly, the photocarrier generation and recombination processes that occur at earliest times are affected most by photobleaching. Combining these transient insights with the relative changes in $\varphi \sum \mu_{\text{sat}}$ (i.e., biggest drop for the IEICO-4F blend), we seek to more clearly understand the origins (and more importantly the different origins from different acceptors) behind these observations using additional information provided by the complementary techniques in our multimodal approach.

2.3. Chemistry—Photoinduced Changes via XPS. 2.3.1. Oxygen Uptake. Time- and accumulated photon dose-dependent changes in chemical environments were evaluated using X-ray photoelectron spectroscopy (XPS), which allows for investigation of reporter atoms on individual moieties of the push—pull architecture and in some cases, chemical resolution between donor and acceptor materials. Using XPS, the C 1s, O 1s, N 1s, S 2p, and F 1s (where applicable) corelevel spectra were taken to investigate chemical changes accompanying photobleaching. We first consider the uptake of (chemically bonded) oxygen in each of the films in dark and light ambient conditions. Figure 4a—e shows the percent

atomic concentrations for as-cast and δ -degraded films, as well as films left in the dark and under illumination for 120 h for the neat materials and blends.

Briefly, the total atomic concentration of oxygen was quantified to provide a first approximation of underlying photooxidation chemistry. In the PDPP4T film (Figure 4a) the oxygen concentration increases from 2.2% (as-cast) to 8.4% (δ degraded), corresponding to an increase from two to six oxygen atoms on average per monomer. We correlate this oxygen uptake with the ~20% loss in FA and note that it occurred in approximately 2.5 h, though we remind that time is not a substantial reactant. The oxygen concentration of 19.8% after 120 h corresponds to completely photobleached PDPP4T (occurring after only 20 h). We note that films cast from chlorobenzene (all except neat PDPP4T) had a small amount of silicone contamination from solution processing that contributes to the O 1s quantification.³⁵ A ~20% loss in FA of the neat acceptors for δ -degraded setpoints could not be reached in reasonable time frames due to their relative stability; thus, partial degradation setpoints were used analogous to the blends. IEICO-4F (Figure 4b) demonstrated much lower oxygen uptake, only increasing from as-cast concentrations by 2.2% after 4 h, and by 4.5% after 120 h, while also retaining color and absorption. We observed only a \sim 30% loss in peak FA over the full 120 h (Figure S2). This marginal uptake and FA loss imply that IEICO-4F is highly resistant to photooxidation. However, as shown in Figure 4c, PC60BM readily exhibited oxygen uptake, demonstrating a 15.3% increase in concentration after 24 h and a 19% increase after 120 h. Yet PC60BM had negligible changes to color and absorption across measured wavelengths (Figure S3), implying that the chromophore functionality of PC60BM is highly resilient to the addition of chemically bonded oxygen.

The \sim 20% loss in FA measured at the wavelength associated with the PDPP4T 0-1 transition (715 nm) in both blends indicates the degree to which photoinduced chemical changes

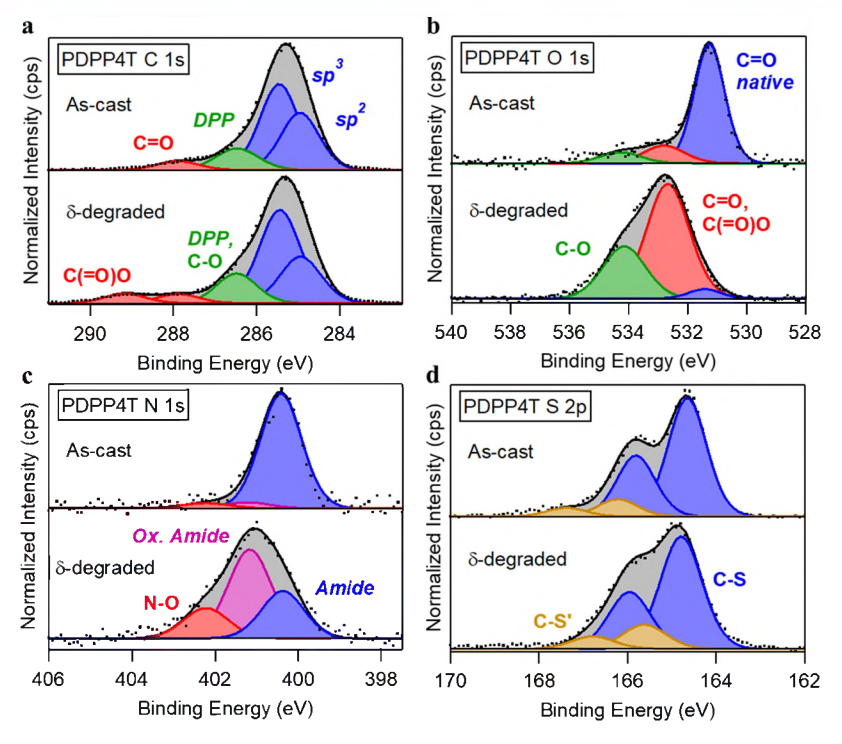


Figure 5. (a) C 1s, (b) O 1s, (c) N 1s, and (d) S 2p core-level XPS spectra for as-cast and δ-degraded PDPP4T.

Table 1. Chemical Assignments to X-ray Photoelectron Spectroscopy Peak Fits in Figure 5^a

PDPP4T	XPS peak fits		As-cast		δ -degraded		
orbital	assignment	BE (eV)	FWHM (eV)	area (%)	BE (eV)	FWHM (eV)	area (%)
Carbon 1s	sp2	284.95	1.07	32.3	284.95	1.15	24.8
	sp3	285.45	1.07	48.4	285.45	1.15	49.6
	C-O	286.50	1.20	13.7	286.50	1.11	15.4
	C=O	287.90	1.20	5.7	287.90	1.12	5.0
	C(=O)O				289.15	1.15	5.2
Oxygen 1s	C=O native	531.25	1.20	75.6	531.40	1.26	4.0
	C=0, C(=0)0	532.83	1.60	15.0	532.66	1.69	66.0
	C-O	534.30	1.60	9.4	534.14	1.69	30.0
Nitrogen 1s	Amide	400.40	1.14	90.2	400.40	1.18	27.9
	Ox. Amide	401.20	1.21	5.1	401.20	1.21	53.3
	N-O	402.20	1.27	4.7	402.20	1.25	18.9
Sulfur 2p	C-S 3/2	164.65	1.00	57.4	164.80	1.09	54.0
	C-S 1/2	165.81	1.00	29.5	165.96	1.09	27.5
	C-S' 3/2	166.20	1.05	8.7	165.60	1.14	12.2
	C-S' 1/2	167.36	1.05	4.4	166.76	1.14	6.3

^aS 2p spin-orbit components fit with a 2:1 intensity ratio for the S 2p_{3/2} and S 2p1/2 and 1.16 eV peak separation.

disrupted chromophore functionality and we reemphasize that PDPP4T experienced this particular degradation mechanism equivalently in both blends by the δ -degraded setpoint. Further, the oxygen concentration in the PDPP4T:IEICO-4F (Figure 4d) blend increased from 6.3 to 11.9% with degradation but increased from 6.8 to 18.0% in the blend with PC₆₀BM (Figure 4e). We note that the PDPP4T:IEICO-4F blend was photodegraded for almost twice as long as the fullerene blend and accumulated almost 4 times the photon dose, to achieve the ~20% loss in FA, and yet still had a lower oxygen uptake. Yet, the fullerene blend retained a greater percentage of optoelectronic performance as measured by TRMC, indicating that photooxidation is not the dominating degradation mechanism.

Figure 4f shows the oxygen content for all films vs APD, and the constant increase of the PDPP4T fit suggests that the polymer continues to photo-oxidize until completely bleached. The acceptors, however, exhibit different behavior: both appear to reach a saturation of oxygen content, approximately 10% (atomic concentration) for IEICO-4F and 25% for $PC_{60}BM$, though the probability of a photoinduced oxygen reaction in the fullerene is higher, as the material reaches its saturation point at much lower doses than the nonfullerene. Consistent with the stabilizing effect of the acceptors on PDPP4T absorption observed with the AIPS, the blended heterojunction oxygen contents also reach an oxygen saturation with photon dose. This is consistent with the proposed hypothesis that the near-pure, amorphous phase of the donor is particularly susceptible to degradation. Alter-

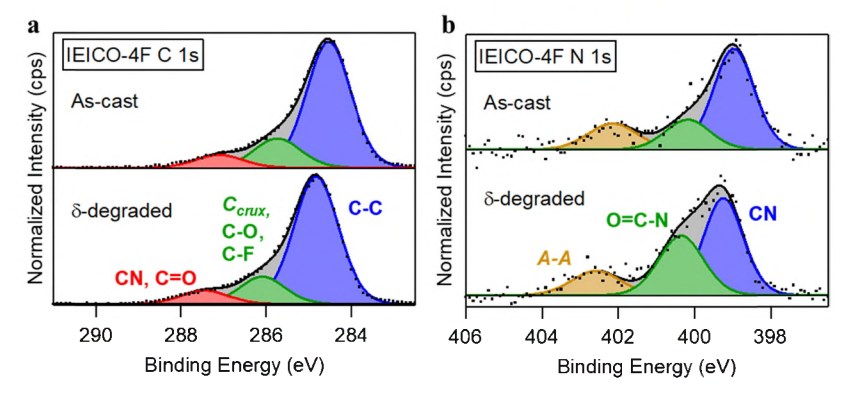


Figure 6. (a) C 1s and (b) N 1s core-level XPS spectra for as-cast and δ -degraded IEICO-4F.

natively, when acceptors are in proximity, or with efficient charge transfer pathways to the donor, enabling electron scavenging before the radical-initiated oxygen reaction can occur; the result of which are domains of the donor "protected" from photooxidation that we observed as continued absorption at the 0-1 transition in blends far past the 20 h at which neat PDPP4T was completely photobleached. The saturation of oxygen content in the blends, 17% for the IEICO-4F blend and 26% for the PC60BM blend, are thereby predominately from the combination of completely photo-oxidized PDPP4T, from the aforementioned susceptible regions, and saturated acceptor domains. We reiterate that despite the lower oxygen uptake of the IEICO-4F blend, the ability of the active layer to photogenerate separated charges was more greatly reduced than that of the PC60BM blend. We now move beyond quantifications of oxygen addition and take a closer look at specific chemical alterations resulting from photodegradation that may elucidate this incongruent loss in photoconductivity.

2.3.2. Chemical Changes to the Neat Donor Material. Chemical analysis of the neat materials demonstrates the key spectroscopic signatures of each molecular component in the core levels as well as enables some insight into bond breakage and/or formation in the materials. We emphasize herein that quantitative mechanistic descriptions of bond breaking and forming are beyond the scope of this work, but rather, we focus on qualitative assessments to connect the above optical changes to chemical modifications of different functional groups on the polymer and acceptor molecules. We first look to the donor; Figure 5 shows the changes in the C 1s, O 1s, N 1s, and S 2p core levels of neat PDPP4T before and after degradation to the δ -degraded setpoint. Additional core-level spectra for neat PDPP4T, IEICO-4F, PC60BM, as well as blends are provided in the SI, including dark/ambient control data (Figures S8-S12) and full degradation data (Figures S13-S17). For reference, Table 1 provides the relative peak assignments for Figure 5, including the binding energy, full width at half-maximum (FWHM), and percent composition within each core-level spectrum.

In Figure 5a, the as-cast PDPP4T film shows four unique regions in the C 1s. The lower binding energy peaks at \sim 285 and \sim 285.5 eV correspond with sp²- and sp³-hybridized carbons, respectively, and collectively, comprise 80.7% of the total carbon signal. The higher-binding-energy peaks at 286.5 and \sim 288 eV are associated with carbon contributions in the DPP unit, where the latter is due to the amide carbon of the pyrrolidone and correlates with the peak in the O 1s spectrum at \sim 531.3 eV (Figure 5b). ³⁶⁻³⁸ Photooxidation studies on

PBDTTPD,³⁹ PTB7-Th,⁴⁰ PTB7,⁴¹ P3HT,⁴² and PCPDTBT,⁴³ which share chemical structural components with PDPP4T, have shown increases in both C–O and C=O bonds, including evolution of carbonyls, esters, and carboxylic acids. Comparison with the PDPP4T δ-degraded C 1s spectrum shows an increase in peak intensities >286 eV (Figure 5a: green/red). We attribute the increase in the 286.5 eV (Figure 5a: green) to evolution of C–O bonds (oxidation), which appears in O 1s as an increase in the ~534.3 eV peak (Figure 5b: green). Similarly, increases in C 1s greater than 287 eV (Figure 5a: red) originate from carbon species with higher-order bonds with oxygen (carbonyls, carboxylic acids, etc.) that correspond to BEs between 531 and 533 eV (Figure 5b: red) in O 1s.

Recalling the significant increase from two to six oxygen atoms per monomer, the N 1s spectra in Figure 5c show an increased signal intensity at higher BE with degradation, consistent with the reported increase in oxygen uptake and complementing the observation of oxygen addition (through bonds) in the C 1s spectrum, particularly of the carbon species in the DPP unit and alkyl chains. This is supported by the nature of the pull unit to attract electron density, making it more likely a site for a radical attack with oxygen due to electronic and structural distortions. Assuming DPP and/or side chain localized oxidation, the proximity of this reaction to the embedded Nitrogen explain the emergence of Nitrogen species with more tightly bound core electrons. With degradation, the peak at 400.4 eV (Figure 5c: blue) that corresponds to the amide (O=C-N) groups in the DPP units is reduced and two new peaks at higher BE emerge. Again, the complexities of exact chemical environment are beyond the scope of this work, but we speculate that the peak at 401.2 eV (red) comes from amide N atoms in close proximity to oxidized C species, convolving contributions from alkyl chain and amide groups. Subsequently, considering the relationship of increased nucleophile BE with degree of oxygen interaction, combined with identification of the N atom to be prone to electrophilic attack, we associate the peak at 402.2 eV (green) with nitro compounds (direct N-O bonding). 24,44 Direct oxidation of the N atoms necessitates a lost bond with an adjacent C, resulting in an opened DPP unit or loss of alkyl chain, and we note that chemical alterations of this magnitude would likely disrupt chromophore functionality and contribute to the \sim 20% loss of the 0–1 transition. We highlight that the identified nitro compounds, likely associated with opened DPP units, contribute to 18.9% of the N 1s signal.

The S 2p spectra consist of doublets arising from spin—orbit coupling, resulting in S $2p_{3/2}$ and S $2p_{1/2}$ with a fixed ratio of

Table 2. Chemical Assignments to X-ray Photoelectron Spectroscopy Peak Fits in Figure 6

IEICO-4F	F XPS peak fits		As-cast		δ -degraded			
orbital	assignment	BE (eV)	FWHM (eV)	area (%)	BE (eV)	FWHM (eV)	area (%)	
Carbon 1s	C-C	284.54	1.21	73.8	284.83	1.22	75.3	
	C _{crux} , C-O, C-F	285.75	1.27	18.0	286.08	1.23	16.2	
	CN, C=O	287.11	1.30	8.2	287.42	1.30	8.4	
Nitrogen 1s	CN	398.97	1.24	61.1	399.25	1.20	50.1	
	O=C-N	400.20	1.36	19.9	400.37	1.35	34.4	
	A- A	402.15	1.49	19.0	402.58	1.49	15.5	

Table 3. Intermolecular Spacings of Semicrystalline Regions in As-Cast and δ -Degraded Films, the Latter Denoted by Columns with (*)

GIWAXS		PDPP4T				IEICO-4F				$PC_{60}BM$		
observable peaks		q_z (Å)			q_{xy} (Å)	q_z	(Å)	q_{xy} (Å)	q_z	(Å)	q_{xy} (Å)	
degradation product		(100)	(200)	(100)	(200)*	(100)	(100)	(010)*	(010)	(n=1)	$(n = 1)^*$	(n = 1)
As-cast	PDPPP4T	23.27	11.42									
	IEICO-4F						3.41		20.94			
	PC ₆₀ BM									8.49		8.49
	PDPP4T:IEICO-4F						3.41		20.27			
	PDPP4T:PC ₆₀ BM	21.67	11.02			22.44						8.49
δ -degraded	PDPP4T	23.27	11.64	16.98	9.67							
	IEICO-4F							15.71	20.94			
	PC ₆₀ BM									9.24	16.11	
	PDPP4T:IEICO-4F				9.52		3.41	15.71	20.27			
	PDPP4T: $PC_{60}BM$	21.67	11.02			22.44						8.49

2:1 in height, with a relative binding energy difference of 1.16 eV and equivalent FWHM. In Figure 5d, we observe a decrease in the higher-binding-energy species, with the S 2p_{3/2} shifting from 166.2 eV for the as-cast film (gold) to 165.6 eV for the δ degraded setpoint, although there is almost no shift for the S 2p_{3/2} peak ascribed to the thiophene units. As oxidation has been identified to be occurring on the pull (nitrogencontaining) unit of the push-pull polymer, we correlate this with minimal oxidation of the thiophene units of the push component. We hypothesize that the shift in the S 2p minority species from the high-BE-tail state toward lower BE arises from the redistribution of electron density due to the addition of chemically bonded oxygen to the pull units. We cannot rule out the presences of sulfates; when degraded for 120 h (Figure S13), far beyond the δ -degraded setpoint, we observe the emergence of new sulfur species consistent with oxidized sulfur and/or ring opening of thiophene units as have been identified in previous reports for thiophene containing organic semi-conductors. 20,41-43,45

2.3.3. Chemical Changes to the Neat Acceptor Materials and Blended Heterojunctions. We look next to the XPS of the neat acceptors. Figure 6 shows the changes in the C 1s and N 1s core levels of neat IEICO-4F before and after degradation to the δ -degraded setpoint. For reference, Table 2 provides the relative peak assignments for Figure 6, including the binding energy, FWHM, and percent composition within each corelevel spectrum.

With only a 2.2% increase in oxygen content, the photoinduced chemical changes to the IEICO-4F C 1s corelevel spectra in Figure 6a are negligible and the S 2p and F 1s spectra were unaffected (Figure S14). We attribute the C 1s peak at \sim 284.5 eV (blue) to sp²- and sp³-hybridized carbons, the peak at \sim 286 eV (green) to native C–O and C–F groups as well as contributions from crux carbons in the indacenodithiophene core and indanone endcaps, and the

peak >287 eV (red) to carbonyl and nitrile groups. In the N 1s spectra in Figure 6b, we observe a nitrile (C≡N) (blue) peak at ~399 eV and a peak at 402.5 eV (gold) that is associated with intermolecular interactions between accepting units (A-to-A aggregation) of the nonfullerene molecules, 46 consistent with the observed semicrystalline regions of face-on IEICO-4F. Additionally, there is an increase in relative intensity of the peak at ~400.3 eV (Figure 6b: green) corresponding to an oxidized nitrile group, identified as a chemical reaction site of oxygen with similarly structured NFAs, 47 and consistent with the BE of the amide group previously identified for PDPP4T. As discussed later, when incorporating X-ray scattering techniques, this peak is attributed to underlying chemical changes that alter the molecule's miscibility and resulting A-to-A aggregation behavior. This result could have significant impact in the broader area of NFA-based materials, as oxidation of the accepting units on the periphery of the molecule is critical for packing and charge transfer in blended heterojunctions, which could in part explain the significant decrease in observed photoconductivity in TRMC.

The fullerene acceptor, $PC_{60}BM$, shows photooxidation as cage reactions with oxygen in the C 1s and O 1s spectra (Figure S15) consistent with the literature. ^{19,43,48} The blended heterojunction spectra (Figures S16 and S17) exhibit peaks consistent with linear combinations of the donor spectra with those of the acceptors and no new peaks are distinguishable that would indicate strong chemical interactions. The changes to blend spectra with degradation are also consistent with a combination of neat material degradation behavior, affirming that the qualitative degradation mechanisms identified for neat materials are active in the blends. In summary, XPS has revealed specific degradation-induced chemical alterations to each material in the blends: PDPP4T shows clear oxidation of the DPP pull component; IEICO-4F exhibits oxidation on its accepting nitrile endcaps; and $PC_{60}BM$ readily oxidizes on the

cage surface. We note that while these observations and quantifications of oxygen uptake do not explain the incongruent loss in photoconductivity (greater oxygen uptake but less photoconductivity loss in the fullerene blend), chemical degradation taken in context with measured changes in phase indicate a more clear picture for stability.

2.4. Microstructure—Physical Morphology Changes via GIXD. The microstructure of an OPV active layer is critically important for optoelectronic operation and X-ray diffraction, or scattering, techniques can reveal these morphological pictures. 8,14,49,50 The intermolecular spacings of semicrystalline regions in the neat and blended films were investigated using grazing-incidence wide-angle X-ray scattering (GIWAXS). The two-dimensional detector images converted to q-space for as-cast and δ -degraded films are shown in Figure S18, and the integrated cake slices in the q_z (out-of-plane) and q_{xy} (in-plane) directions are shown in Figure S19. The intermolecular spacings in angstroms from all observable peaks are given in Table 3 for as-cast and δ degraded films. Additionally, the average size of acceptor domains in the blended heterojunctions was investigated using grazing-incidence small-angle X-ray scattering (GISAXS). This technique uses the contrasting electron density between phases within a blended film to identify the average domain size, herein given as average diameters, in the range of ca. 3-80 nm. Two-dimensional GISAXS images are shown in Figure S20, and the corresponding one-dimensional intensity vs q-space figures with unified fits are given in Figure S21.

2.4.1. Microstructure of Neat Materials—Intermolecular Spacings. As-cast PDPP4T shows an out-of-plane (100) spacing of 23.27 Å and the accompanying (200) second-order Bragg diffraction peak. The polymer adopts an edge-on orientation as the (100) is attributed to lamellar packing and no peaks associated with the π - π stacking direction are observed. Upon degradation, the out-of-plane PDPP4T intermolecular spacing peaks have reduced intensities and there is a new (100) spacing of 16.98 Å with an accompanying (200) peak, suggestive of a chemical alteration (oxidation) on the alkyl side chains of the edge-on oriented polymer.

As-cast IEICO-4F exhibits an out-of-plane 3.41 Å $\pi-\pi$ stacking peak and an in-plane 20.94 Å lamellar peak consistent with previous reports that indicate a face-on orientation. $^{52-54}$ Upon degradation, the $\pi-\pi$ stacking peak is reduced or broadened to where it is no longer distinguishable while the lamellar peak is still present, but the relative intensity has been significantly reduced. We attribute this loss in crystallinity to the oxidation of the peripheral nitrile groups observed with XPS disrupting and reducing crystalline regions. A new out-of-plane peak of 15.71 Å also arises with degradation, supporting our hypothesis of chemically induced IEICO-4F molecular reorganization with the emergence of some edge-on crystalline regions.

For PC₆₀BM, both the out-of-plane and in-plane directions show the characteristic 8.49 Å (n = 1) intermolecular spacing of the fullerene. Upon degradation, this peak is lost and two new peaks, 16.11 and 9.24 Å, appear in the out-of-plane direction. The slightly increased intermolecular spacing from 8.49 to 9.24 Å is evidence of fullerene cage reactions with oxygen, consistent with the literature and previously mentioned XPS oxygen concentration increases. PC₆₀BM is also known to readily dimerize when photodegraded, and the 16.11 Å spacing (\sim 2 × the as-cast spacing) supports this occurrence.

2.4.2. Microstructure of Blended Heterojunctions. 2.4.2.1. Intermolecular Spacings of Semicrystalline Regions. In GIWAXS, the as-cast PDPP4T:IEICO-4F blend exhibits both the out-of-plane and in-plane peaks of IEICO-4F but there is no evidence of PDPP4T crystallization. Upon degradation, these peaks are unaltered, but a lamellar peak associated with PDPP4T and a 15.71 Å peak corresponding to face-on IEICO-4F emerge, indicating subtle microstructural changes. The PDPP4T:PC60BM blend shows the (100) and (200) peaks of edge-on polymer in the out-of-plane direction, now corresponding to a slightly reduced spacing of 21.67 Å. In the in-plane direction, the (n = 1) peak of PC₆₀BM is apparent as well as a lamellar peak of 22.44 Å, indicating the presence of some face-on PDPP4T. Again, the identified peaks are unaltered with degradation but while not observable, some PC₆₀BM dimerization is likely occurring in the fullerene blend and contributing to reduction in photoconductivity $(\phi \sum \mu)$, as supported by carrier mobility losses in devices. 58 These results indicate that while both acceptors form semicrystalline regions when blended with PDPP4T, the donor however only does so with PC₆₀BM. Additionally, the features corresponding to degradation byproducts of neat materials are significantly reduced in blends, supplementing observations of color (AIPS) and chemical (XPS) stability enhancements in blends with morphological rigidity. However, while the microstructure of the fullerene blend was largely unaltered with degradation, the nonfullerene blend shows evidence of molecular reorganiza-

2.4.2.2. Average Domain Sizes. The PDPP4T:IEICO-4F blend did not have domains detectable within the ca. 3-80 nm range of GISAXS, but upon degradation, new domains with an average diameter of 16.4 nm were detected. GIWAXS results indicated the crystalline presence of only the nonfullerene acceptor in both as-cast and δ -degraded films, which suggests that the blend morphology was initially amorphous PDPP4T with highly intercalated small grains (<3nm) of pure IEICO-4F acting as defects impeding the crystallization of the polymer. It is highly unlikely that domains existed in the as-cast film that were greater than 80 nm as this would result in large domains of pure PDPP4T that would be expected to crystallize. Further, inspection with a microscope revealed a uniform film and no visible domains were detected. Photodegradation then provided the driving force for morphological rearrangement and increased IEICO-4F miscibility allowing the small molecule acceptor to phase segregate from the amorphous polymer donor and grow to larger domains, although not equivalent to the pure IEICO-4F material. In Section 2.4.1, the increased miscibility of IEICO-4F and subsequent molecular freedom in the neat film disrupted the semicrystalline regions as detected by GIWAXS. Here, increased miscibility has allowed for phase segregation increasing the average size of IEICO-4F domains, domains that are not necessarily semicrystalline, and we do not observe an increase in relative intensity of the NFA semicrystalline peaks, consistent with neat IEICO-4F behavior. Phase instability has been previously reported for polymer:IEICO-4F blends,60 including direct contrast of NFA blend instability with the relative stability of fullerene blends.32

The PDPP4T:PC₆₀BM blend has average domain sizes of 18.0 and 16.9 nm for as-cast and δ -degraded films, respectively. As the GIWAXS results indicate the crystalline presence of both donor and acceptor materials in both films, the morphology of this blend can be described as a semicrystalline

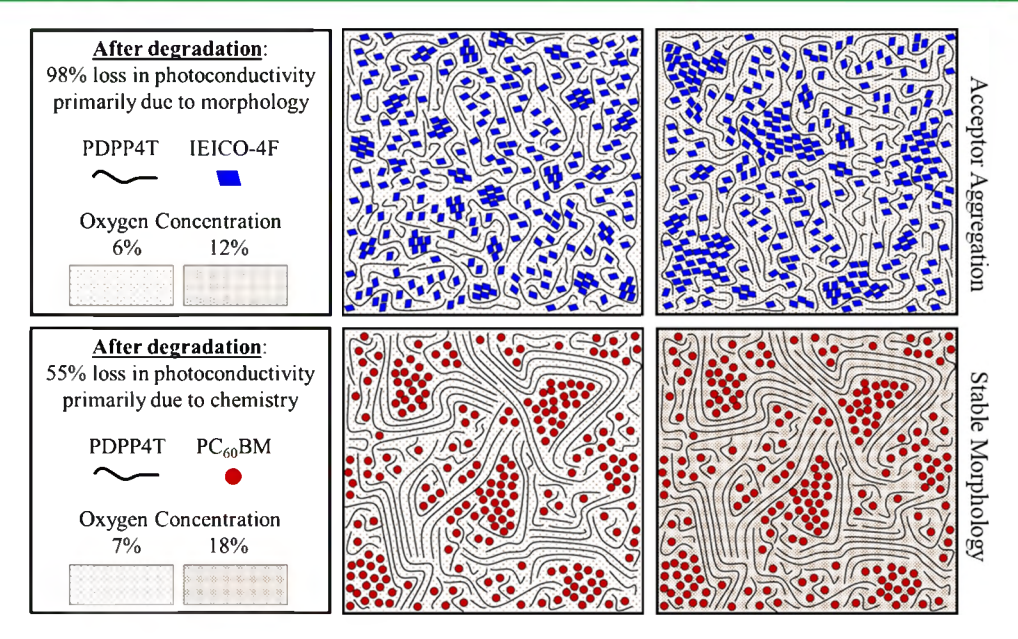


Figure 7. As-cast to δ -degraded (left to right) polymer:nonfullerene (top) and polymer:fullerene (bottom) blends incorporating multimodal experimental results.

polymer matrix with 17-18 nm domains of $PC_{60}BM$, consistent with prior analysis of polymer:fullerene thin films. 55,61,62 This blend morphology saw little change upon degradation, indicating a stable physical arrangement, despite many chemical changes. The significant phase segregation observed in the IEICO-4F blend would be consistent with a significant loss in photoconductivity since the interfacial area between donor and acceptor is critical for exciton disassociation.

3. CONCLUSIONS

In summary, the combined results (TRMC, XPS, GIWAXS, GISAXS) of the multimodal approach for the two systems are summarized in Figure 7.

The ~20% loss in FA measured at the wavelength associated with the PDPP4T 0-1 transition (715 nm) in both blends indicates the degree to which photoinduced chemical changes disrupted chromophore functionality, and we remind that PDPP4T experienced this particular degradation mechanism equivalently in both blends by the δ -degraded setpoint. Further, the oxygen concentration in the PDPP4T:IEICO-4F blend increased from 6 to 12% with degradation but increased from 7 to 18% in the blend with PC₆₀BM. Despite the higher oxygen uptake of the fullerene blend and equivalent donor absorption degradation, PDPP4T:PC60BM only lost 55% of the photoconductive performance while the IEICO-4F blend lost 98%. We attribute this incongruent loss in photoconductivity to phase instability of the nonfullerene blend. A multimodal approach to degradation must be self-consistent across experimental results and the interrelationships in this material system between chromophore stability, chargegeneration capacity, chemical makeup, and microstructure all agree. Specifically, we note that the phase segregation of IEICO-4F evident in GISAXS is consistent with changes in intermolecular spacings (GIWAXS) and is caused by oxidation of the nitrile group as observed in XPS. The loss of D:A interfacial area combined with photooxidation of PDPP4T (observed in XPS and as absorption/color changes in AIPS) resulted in the significant loss in photoconductive performance

(TRMC). Similarly, the phase (GISAXS) and microstructure (GIWAXS) stability of the $PC_{60}BM$ blend supports greater retention of photoconductive performance (TRMC), while photooxidation evident in XPS and AIPS is responsible for the observed loss. These results could not have been obtained by solely investigating color stability, performance, chemical alterations, or microstructure, demonstrating why a multimodal approach is necessary for a complete understanding of OPV active layer degradation.

4. EXPERIMENTAL SECTION

4.1. Sample Preparation. Preliminary work was performed with PDPP4T provided by 1-Material, $PC_{60}BM$ provided by Nano-C, and a sample of IEICO-4F from Solarmer Energy, Inc. PDPP4T and $PC_{60}BM$ were later purchased from Ossila and IEICO-4F from 1-Material. IEICO-4F and $PC_{60}BM$ films were spin-cast from 10 mg/mL solutions in chlorobenzene and PDPP4T films were cast from a 5 mg/mL solution in chloroform. Blended heterojunctions were cast by mixing solutions with a solute weight donor:acceptor ratio of 1:1. Approximately 50–150 uL of solution was deposited for spin-coating and the general spin-coating recipe used for all films with slight variations is as follows: (4000 rpm for 1 s)–(800 rpm for 45 s)–(4000 rpm for 1 s). All solution processing took place inside nitrogen gloveboxes and films were only exposed to light or ambient conditions when undergoing experimentation.

4.2. Automated In Situ Photobleaching Spectrometer. Samples were exposed to indoor ambient conditions with light exposure of 120 mW/cm² from a four-bulb DC halogen lamp (Sylvania 58321) array. The samples were rotated continuously during photobleaching to ensure uniform exposure and spectra were taken at set intervals. The fraction of light absorbed (FA) spectra was calculated from the fraction reflected (FR) and fraction transmitted (FT) as FA = 1-FT-FR. FR and FT spectra were collected by separate spectrometers (Ocean Optics HR2000) fitted with a "six around one" reflectance probe (Ocean Optics R400-7-SR) and a collimating lens, respectively. The reflectance reference was an aluminum first surface mirror. The accumulated photon dose was calculated using eq 3

accumulated photon $dose(t_i)$

$$= \int_{t=t_0}^{t=t_i} \int_{\lambda_1}^{\lambda_2} FA(\lambda, t) \cdot I_{L_{\text{photon}}}(\lambda) d\lambda dt$$
(3)

where $I_{\rm L_{photon}}$ is the degradation lamp array's spectral photon flux. A sixinch integrating sphere (Optronic Labs OL IS-670) fitted with silicon (Soma S-2441C) and InGaAs (Spectral evolution LF1250) diode arrays were used to gather the spectral irradiance data of the photobleaching light source, which was converted to photon flux using the equation

$$I_{L_{\rm photon}}(\lambda) = \frac{{\rm spectral\; irradiance}(\lambda)^* \lambda}{hc} \tag{4}$$

4.3. Time-Resolved Microwave Conductivity. Samples were spin-cast onto fused quartz substrates (11 mm × 25 mm × 1 mm) with ground and polished edges and secured in a brass X-band microwave cavity. The cavity has a grating that is transparent to the 5 ns laser pulses that optically excite the sample to photogenerate carriers but is reflective to microwaves. The light source is a Qswitched Nd:YAG laser operating at 355 nm that goes through an optical parameter oscillator (OPO) for wavelength selection. A NIR wavelength of 800 nm was used to excite the samples using the idler beam. A beam expander was placed before the microwave cavity so that each laser pulse fully illuminates the sample. A series of neutral density filters were used to attenuate the laser so that photoconductance is measured for light intensities over several orders of magnitude. The mobile carriers and their decay by recombination are measured as time-resolved changes in absorbed microwave power. The resulting transients are then fit with an exponentially modified Gaussian (EMG) function.^{33,34} The transient change in photoconductance, $\Delta G \exp(t)$, is given by eq 5

$$\Delta G \exp(t) = -\frac{1}{K} \frac{\Delta P(t)}{P} \tag{5}$$

where $\Delta P(t)$ is the change in microwave power due to absorption of microwaves by the generated carriers and K is a calibration factor experimentally determined from resonance characteristics of the microwave cavity and the dielectric properties of the sample. The end-of-pulse or peak photoconductance, $\Delta G_{\rm EOP}$, can be related to the product of the carrier generation yield, ϕ , and the sum of the high-frequency electron, $\mu_{\rm e}$, and hole, $\mu_{\rm h}$, mobilities in the film, $\sum \mu$, by the equation

$$\Delta G_{\text{EOP}} = \beta \ q_{\text{e}} I_0 \ FA \ \phi(\mu_{\text{e}} + \mu_{\text{h}}) \tag{6}$$

where $\beta=2.2$ is the ratio of the interior dimensions of the waveguide, $q_{\rm e}$ is the electronic charge, I_0 is the incident photon flux of the excitation pulse, and FA is the fractional absorptance of the film at the excitation wavelength. The $\Delta G_{\rm EOP}$ increases linearly with I_0 at low intensities but becomes sublinear as higher-order processes and carrier generation yield limits become significant at higher intensities. The TRMC figure of merit is the yield-mobility product, $\phi \sum \mu$. Sample photoconductance can then either be evaluated by extracting $\phi \sum \mu$ at specific intensities or by fitting $\phi \sum \mu$ to the low-intensity region where it is independent of absorbed photon flux.

4.4. X-ray Photoelectron Spectroscopy. XPS was performed with a Kratos Axis Ultra X-ray photoelectron spectrometer with a 1486.6 eV monochromatic Al K α source at a base pressure of 10^{-8} Torr. Photoelectrons were collected and analyzed using a hemispherical analyzer and a photodiode array. A 20 eV pass energy was used for all element-specific acquisitions, and the resulting spectra were corrected using the Shirley background. Quantifications for percent atomic concentration were done by area.

4.5. Grazing-Incidence Wide-Angle X-ray Scattering. GI-WAXS experiments were carried out on beamline 11-3 at the Stanford Synchrotron Radiation Lightsource (SSRL), equipped with a two-dimensional Rayonix MX225 CCD area detector. The incident angle of measurement was ca. 0.11–0.12° and the beam energy was kept at 12.7 keV. A LaB6 standard sample was used to calibrate the wavelength and sample-detector distance. The obtained two-dimensional images were converted from intensity versus pixel position to intensity versus reciprocal space (q-space) using WAXS tools and Nika macros in Igor 6.37.⁶³ Two-dimensional images were reduced to one-dimensional intensity versus qz- and qxy-space by integration of

cake segments taken from chi of 0-15 and $73-88^{\circ}$, respectively. Intermolecular spacings (d) were calculated from the inverse coordinate by eq 7^{50}

$$d_{bkl} = 2\pi/q \tag{7}$$

4.6. Grazing-Incidence Small-Angle X-ray Scattering. GISAXS experiments were carried out on beamline 1–5 at SSRL, equipped with a Rayonix SX165 area detector. The sample-to-SAXS detector distance was 3 m, and an X-ray energy of 8 keV at an incidence angle of 0.18° was used. Calibration was done using silver AgBe, and data was fit in Igor 6.37 with the Irena SAS modeling macros using the unified fit model. 64

ASSOCIATED CONTENT

Supporting Information

The Supporting Information is available free of charge at https://pubs.acs.org/doi/10.1021/acsami.1c12321.

AIPS waterfall plots for neat and blended heterojunctions; AIPS lamp profile used for photobleaching; TRMC transients with biexponential fits; additional XPS core-level spectra for neat and blended films, including dark controls and additionally degraded samples; and additional GIWAXS and GISAXS 2D detector images and associated 1D integrations (PDF)

AUTHOR INFORMATION

Corresponding Authors

Bryon W. Larson – Chemistry and Nanoscience Center, National Renewable Energy Laboratory, Golden, Colorado 80401, United States; orcid.org/0000-0002-0934-987X; Email: bryon.larson@nrel.gov

Erin L. Ratcliff — Department of Materials Science and Engineering, University of Arizona, Tucson, Arizona 85721, United States; Department of Chemical and Environmental Engineering and Department of Chemistry and Biochemistry, University of Arizona, Tucson, Arizona 85721, United States; Orcid.org/0000-0002-2360-8436;

Email: ratcliff@arizona.edu

Author

Michael A. Anderson – Department of Materials Science and Engineering, University of Arizona, Tucson, Arizona 85721, United States

Complete contact information is available at: https://pubs.acs.org/10.1021/acsami.1c12321

Author Contributions

The manuscript was written through contributions of all authors. All authors have given approval to the final version of the manuscript.

Notes

The authors declare no competing financial interest.

ACKNOWLEDGMENTS

The authors express their sincere gratitude to Paul Lee (UArizona), Dr. Christopher Tassone (SSRL), and Dr. Sami Sainio (SSRL) for training and assistance in data collection for XPS, GISAXS, and GIWAXS, respectively. Materials, supplies, XPS facility time, and ELR were supported by the National Science Foundation under grant awards DMR-1608289 and DMR-2003631. M.A.A. acknowledges partial support from the National Science Foundation under grant awards DGE-1735173, DMR-1608289, and DMR-2003631. Travel to

Research Article

NREL was supported by the University of Arizona Institute for Energy Solutions. Use of the Stanford Synchrotron Radiation Lightsource, SLAC National Accelerator Laboratory, is supported by the U.S. Department of Energy, Office of Science, Office of Basic Energy Sciences under Contract No. DEAC02-76SF00515. A portion of this work was conducted in the Nano Fabrication Center at the University of Arizona. This work was authored in part by the National Renewable Energy Laboratory (NREL), operated by Alliance for Sustainable Energy, LLC, for the U.S. Department of Energy (DOE) under Contract No. DE-AC36-08GO28308. The views expressed in the article do not necessarily represent the views of the DOE or the U.S. Government. B.W.L. acknowledges partial support by the ARPA-E DIFFERENTIATE program under grant no. DE-AR0001215.

REFERENCES

- (1) Bronstein, H.; Nielsen, C. B.; Schroeder, B. C.; McCulloch, I. The Role of Chemical Design in the Performance of Organic Semiconductors. *Nat. Rev. Chem.* **2020**, *4*, 66–77.
- (2) Espinosa, N.; Hösel, M.; Angmo, D.; Krebs, F. C. Solar Cells with One-Day Energy Payback for the Factories of the Future. *Energy Environ. Sci.* **2012**, *5*, 5117–5132.
- (3) Emmott, C. J. M.; Röhr, J. A.; Campoy-Quiles, M.; Kirchartz, T.; Urbina, A.; Ekins-Daukes, N. J.; Nelson, J. Organic Photovoltaic Greenhouses: A Unique Application for Semi-Transparent PV? *Energy Environ. Sci* **2015**, *8*, 1317–1328.
- (4) Liu, Y.; Cheng, P.; Li, T.; Wang, R.; Li, Y.; Chang, S.-Y.; Zhu, Y.; Cheng, H.-W.; Wei, K.-H.; Zhan, X.; Sun, B.; Yang, Y. Unraveling Sunlight by Transparent Organic Semiconductors toward Photovoltaic and Photosynthesis. *ACS Nano* **2019**, *13*, 1071–1077.
- (5) Friman Peretz, M.; Geoola, F.; Yehia, I.; Ozer, S.; Levi, A.; Magadley, E.; Brikman, R.; Rosenfeld, L.; Levy, A.; Kacira, M.; Teitel, M. Testing Organic Photovoltaic Modules for Application as Greenhouse Cover or Shading Element. *Biosys. Eng.* **2019**, *184*, 24–36
- (6) Zhang, M.; Zhu, L.; Zhou, G.; Hao, T.; Qiu, C.; Zhao, Z.; Hu, Q.; Larson, B. W.; Zhu, H.; Ma, Z.; Tang, Z.; Feng, W.; Zhang, Y.; Russell, T. P.; Liu, F. Single-Layered Organic Photovoltaics with Double Cascading Charge Transport Pathways: 18% Efficiencies. *Nat. Commun.* 2021, 12, No. 309.
- (7) Cui, C. Recent Progress in Fused-Ring Based Nonfullerene Acceptors for Polymer Solar Cells. Front. Chem. 2018, 6, No. 404.
- (8) Wang, Y.; Lee, J.; Hou, X.; Labanti, C.; Yan, J.; Mazzolini, E.; Parhar, A.; Nelson, J.; Kim, J.; Li, Z. Recent Progress and Challenges toward Highly Stable Nonfullerene Acceptor-Based Organic Solar Cells. *Adv. Energy Mater.* **2021**, *11*, No. 2003002.
- (9) Garner, L. E.; Nellissery Viswanathan, V.; Arias, D. H.; Brook, C. P.; Christensen, S. T.; Ferguson, A. J.; Kopidakis, N.; Larson, B. W.; Owczarczyk, Z. R.; Pfeilsticker, J. R.; Ramamurthy, P. C.; Strauss, S. H.; Boltalina, O. V.; Braunecker, W. A. Photobleaching Dynamics in Small Molecule vs. Polymer Organic Photovoltaic Blends with 1,7-Bis-Trifluoromethylfullerene. J. Mater. Chem. A 2018, 6, 4623–4628.
- (10) Savenije, T. J.; Ferguson, A. J.; Kopidakis, N.; Rumbles, G. Revealing the Dynamics of Charge Carriers in Polymer:Fullerene Blends Using Photoinduced Time-Resolved Microwave Conductivity. *J. Phys. Chem. C* **2013**, *117*, 24085–24103.
- (11) Reid, O. G.; Moore, D. T.; Li, Z.; Zhao, D.; Yan, Y.; Zhu, K.; Rumbles, G. Quantitative Analysis of Time-Resolved Microwave Conductivity Data. J. Phys. D: Appl. Phys. 2017, 50, No. 493002.
- (12) Li, Y.; Sonar, P.; Murphy, L.; Hong, W. High Mobility Diketopyrrolopyrrole (DPP)-Based Organic Semiconductor Materials for Organic Thin Film Transistors and Photovoltaics. *Energy Environ. Sci.* 2013, 6, 1684.
- (13) Mateker, W. R.; McGehee, M. D. Progress in Understanding Degradation Mechanisms and Improving Stability in Organic Photovoltaics. *Adv. Mater.* **2017**, *29*, No. 1603940.

- (14) Liu, F.; Gu, Y.; Wang, C.; Zhao, W.; Chen, D.; Briseno, A. L.; Russell, T. P. Efficient Polymer Solar Cells Based on a Low Bandgap Semi-Crystalline DPP Polymer-PCBM Blends. *Adv. Mater.* **2012**, *24*, 3947–3951.
- (15) Lee, J.; Cha, H.; Yao, H.; Hou, J.; Suh, Y.-H.; Jeong, S.; Lee, K.; Durrant, J. R. Toward Visibly Transparent Organic Photovoltaic Cells Based on a Near-Infrared Harvesting Bulk Heterojunction Blend. *ACS Appl. Mater. Interfaces* **2020**, *12*, 32764–32770.
- (16) Grossiord, N.; Kroon, J. M.; Andriessen, R.; Blom, P. W. M. Degradation Mechanisms in Organic Photovoltaic Devices. *Organic Electronics* **2012**, *13*, 432–456.
- (17) Salvador, M.; Gasparini, N.; Perea, J. D.; Paleti, S. H.; Distler, A.; Inasaridze, L. N.; Troshin, P. A.; Luer, L.; Egelhaaf, H.-J.; Brabec, C. Suppressing Photooxidation of Conjugated Polymers and Their Blends with Fullerenes through Nickel Chelates. *Energy Environ. Sci.* **2017**, *10*, 2005–2016.
- (18) Hoke, E. T.; Sachs-Quintana, I. T.; Lloyd, M. T.; Kauvar, I.; Mateker, W. R.; Nardes, A. M.; Peters, C. H.; Kopidakis, N.; McGehee, M. D. The Role of Electron Affinity in Determining Whether Fullerenes Catalyze or Inhibit Photooxidation of Polymers for Solar Cells. *Adv. Energy Mater.* **2012**, *2*, 1351–1357.
- (19) Domínguez, I. F.; Distler, A.; Luer, L. Stability of Organic Solar Cells: The Influence of Nanostructured Carbon Materials. *Adv. Energy Mater.* **2017**, *7*, No. 1601320.
- (20) Watts, K. E.; Nguyen, T.; Villers, B. J. T. de.; Neelamraju, B.; Anderson, M. A.; Braunecker, W. A.; Ferguson, A. J.; Larsen, R. E.; Larson, B. W.; Owczarczyk, Z. R.; Pfeilsticker, J. R.; Pemberton, J. E.; Ratcliff, E. L. Stability of Push—Pull Small Molecule Donors for Organic Photovoltaics: Spectroscopic Degradation of Acceptor Endcaps on Benzo[1,2-b:4,5-B']Dithiophene Cores. *J. Mater. Chem. A* **2019**, *7*, 19984—19995.
- (21) Tonga, M. Tunable Optical Properties of Push-Pull Chromophores: End Group Effect. *Tetrahedron Lett.* **2020**, *61*, No. 152205.
- (22) Dou, L.; Liu, Y.; Hong, Z.; Li, G.; Yang, Y. Low-Bandgap Near-IR Conjugated Polymers/Molecules for Organic Electronics. *Chem. Rev.* 2015, 115, 12633–12665.
- (23) Patil, Y.; Misra, R. Rational Molecular Design towards NIR Absorption: Efficient Diketopyrrolopyrrole Derivatives for Organic Solar Cells and Photothermal Therapy. *J. Mater. Chem. C* **2019**, *7*, 13020–13031.
- (24) Grzybowski, M.; Gryko, D. T. Diketopyrrolopyrroles: Synthesis, Reactivity, and Optical Properties. *Adv. Opt. Mater.* **2015**, *3*, 280–320.
- (25) Yamagata, H.; Spano, F. C. Interplay between Intrachain and Interchain Interactions in Semiconducting Polymer Assemblies: The HJ-Aggregate Model. *J. Chem. Phys.* **2012**, *136*, No. 184901.
- (26) Clark, J.; Silva, C.; Friend, R. H.; Spano, F. C. Role of Intermolecular Coupling in the Photophysics of Disordered Organic Semiconductors: Aggregate Emission in Regioregular Polythiophene. *Phys. Rev. Lett.* **2007**, 98, No. 206406.
- (27) Li, M.; Balawi, A. H.; Leenaers, P. J.; Ning, L.; Heintges, G. H. L.; Marszalek, T.; Pisula, W.; Wienk, M. M.; Meskers, S. C. J.; Yi, Y.; Laquai, F.; Janssen, R. A. J. Impact of Polymorphism on the Optoelectronic Properties of a Low-Bandgap Semiconducting Polymer. *Nat. Commun.* **2019**, *10*, No. 2867.
- (28) Larson, B. W.; Ferguson, A. J.; De Villers, B. J. T.; Larsen, R. E. A Device-Independent Screening Technique for Rapidly Identifying Next Generation OPV Materials. In 2017 IEEE 44th Photovoltaic Specialist Conference (PVSC); IEEE: Washington, DC, 2017; pp. 1354–1359.
- (29) Ferguson, A. J.; Larson, B. W.; Tremolet de Villers, B. J.; Braunecker, W. A.; Larsen, R. E. RAMP-Ing the Discovery of High-Performance Organic Photovoltaic Materials (Conference Presentation). In *Organic, Hybrid, and Perovskite Photovoltaics XVIII*, Lee, K.; Kafafi, Z. H.; Lane, P. A., Eds.; SPIE: San Diego, United States, 2017; p 16.
- (30) Saeki, A.; Yoshikawa, S.; Tsuji, M.; Koizumi, Y.; Ide, M.; Vijayakumar, C.; Seki, S. A Versatile Approach to Organic

- Photovoltaics Evaluation Using White Light Pulse and Microwave Conductivity. J. Am. Chem. Soc. 2012, 134, 19035–19042.
- (31) Ghosh, T.; Gopal, A.; Nagasawa, S.; Mohan, N.; Saeki, A.; Nair, V. C. Following the TRMC Trail: Optimization of Photovoltaic Efficiency and Structure-Property Correlation of Thiophene Oligomers. ACS Appl. Mater. Interfaces 2016, 8, 25396-25404.
- (32) Doumon, N. Y.; Dryzhov, M. V.; Houard, F. V.; Le Corre, V. M.; Rahimi Chatri, A.; Christodoulis, P.; Koster, L. J. A. Photostability of Fullerene and Non-Fullerene Polymer Solar Cells: The Role of the Acceptor. ACS Appl. Mater. Interfaces 2019, 11, 8310–8318.
- (33) Holt, J. M.; Ferguson, A. J.; Kopidakis, N.; Larsen, B. A.; Bult, J.; Rumbles, G.; Blackburn, J. L. Prolonging Charge Separation in P3HT-SWNT Composites Using Highly Enriched Semiconducting Nanotubes. *Nano Lett.* **2010**, *10*, 4627–4633.
- (34) Dicker, G.; de Haas, M. P.; Siebbeles, L. D. A.; Warman, J. M. Electrodeless Time-Resolved Microwave Conductivity Study of Charge-Carrier Photogeneration in Regioregular Poly(3-Hexylthiophene) Thin Films. *Phys. Rev. B* **2004**, *70*, No. 045203.
- (35) Carr, J. A.; Nalwa, K. S.; Mahadevapuram, R.; Chen, Y.; Anderegg, J.; Chaudhary, S. Plastic-Syringe Induced Silicone Contamination in Organic Photovoltaic Fabrication: Implications for Small-Volume Additives. ACS Appl. Mater. Interfaces 2012, 4, 2831–2835.
- (36) Gora, M.; Krzywiec, W.; Mieczkowski, J.; Rodrigues Maia, E. C.; Louarn, G.; Zagorska, M.; Pron, A. Alternating Copolymers of Diketopyrrolopyrrole or Benzothiadiazole and Alkoxy-Substituted Oligothiophenes: Spectroscopic, Electrochemical and Spectroelectrochemical Investigations. *Electrochim. Acta* **2014**, *144*, 211–220.
- (37) Ponnappa, S. P.; Liu, Q.; Umer, M.; MacLeod, J.; Jickson, J.; Ayoko, G.; Shiddiky, M. J. A.; O'Mullane, A. P.; Sonar, P. Naphthalene Flanked Diketopyrrolopyrrole: A New Conjugated Building Block with Hexyl or Octyl Alkyl Side Chains for Electropolymerization Studies and Its Biosensor Applications. *Polym. Chem.* **2019**, *10*, 3722–3739.
- (38) Liu, X.; Kong, L.; Du, H.; Zhang, Y.; Zhao, J.; Xie, Y. Synthesis and Electrochromic Properties of Electrochromic Polymers Based on Propylenedioxythiophene, Diketopyrrolopyrrole and Benzodithiophene Units. *Organic Electronics* **2019**, *64*, 223–235.
- (39) Tournebize, A.; Gardette, J.-L.; Taviot-Guého, C.; Bégué, D.; Arnaud, M. A.; Dagron-Lartigau, C.; Medlej, H.; Hiorns, R. C.; Beaupré, S.; Leclerc, M.; Rivaton, A. Is There a Photostable Conjugated Polymer for Efficient Solar Cells? *Polym. Degrad. Stab.* **2015**, *112*, 175–184.
- (40) Kim, S.; Rashid, M. A. M.; Ko, T.; Ahn, K.; Shin, Y.; Nah, S.; Kim, M. H.; Kim, B.; Kwak, K.; Cho, M. New Insights into the Photodegradation Mechanism of the PTB7-Th Film: Photooxidation of π-Conjugated Backbone upon Sunlight Illumination. *J. Phys. Chem. C* **2020**, *124*, 2762–2770.
- (41) Kettle, J.; Ding, Z.; Horie, M.; Smith, G. C. XPS Analysis of the Chemical Degradation of PTB7 Polymers for Organic Photovoltaics. *Organic Electronics* **2016**, *39*, 222–228.
- (42) Hintz, H.; Egelhaaf, H.-J.; Peisert, H.; Chassé, T. Photo-Oxidation and Ozonization of Poly(3-Hexylthiophene) Thin Films as Studied by UV/VIS and Photoelectron Spectroscopy. *Polym. Degrad. Stab.* **2010**, *95*, 818–825.
- (43) Kettle, J.; Waters, H.; Ding, Z.; Horie, M.; Smith, G. C. Chemical Changes in PCPDTBT:PCBM Solar Cells Using XPS and TOF-SIMS and Use of Inverted Device Structure for Improving Lifetime Performance. Sol. Energy Mater. Sol. Cells 2015, 141, 139–147.
- (44) Eng, J.; Hubner, I. A.; Barriocanal, J.; Opila, R. L.; Doren, D. J. X-Ray Photoelectron Spectroscopy of Nitromethane Adsorption Products on Si(100): A Model for N 1s Core-Level Shifts in Silicon Oxynitride Films. *J. Appl. Phys.* **2004**, *95*, 1963–1968.
- (45) Norrman, K.; Madsen, M. V.; Gevorgyan, S. A.; Krebs, F. C. Degradation Patterns in Water and Oxygen of an Inverted Polymer Solar Cell. *J. Am. Chem. Soc.* **2010**, *132*, 16883–16892.

- (46) Li, D.; Zhang, X.; Liu, D.; Wang, T. Aggregation of Non-Fullerene Acceptors in Organic Solar Cells. *J. Mater. Chem. A* **2020**, 8, 15607–15619.
- (47) Guo, J.; Wu, Y.; Sun, R.; Wang, W.; Guo, J.; Wu, Q.; Tang, X.; Sun, C.; Luo, Z.; Chang, K.; Zhang, Z.; Yuan, J.; Li, T.; Tang, W.; Zhou, E.; Xiao, Z.; Ding, L.; Zou, Y.; Zhan, X.; Yang, C.; Li, Z.; Brabec, C. J.; Li, Y.; Min, J. Suppressing Photo-Oxidation of Non-Fullerene Acceptors and Their Blends in Organic Solar Cells by Exploring Material Design and Employing Friendly Stabilizers. J. Mater. Chem. A 2019, 7, 25088–25101.
- (48) Brumboiu, I. E.; Ericsson, L.; Hansson, R.; Moons, E.; Eriksson, O.; Brena, B. The Influence of Oxygen Adsorption on the NEXAFS and Core-Level XPS Spectra of the C ₆₀ Derivative PCBM. *J. Chem. Phys.* **2015**, *142*, No. 054306.
- (49) Zhang, C.; Heumueller, T.; Leon, S.; Gruber, W.; Burlafinger, K.; Tang, X.; Perea, J. D.; Wabra, I.; Hirsch, A.; Unruh, T.; Li, N.; Brabec, C. J. A Top-down Strategy Identifying Molecular Phase Stabilizers to Overcome Microstructure Instabilities in Organic Solar Cells. Energy Environ. Sci. 2019, 12, 1078–1087.
- (50) Rivnay, J.; Mannsfeld, S. C. B.; Miller, C. E.; Salleo, A.; Toney, M. F. Quantitative Determination of Organic Semiconductor Microstructure from the Molecular to Device Scale. *Chem. Rev.* **2012**. *112*. 5488–5519.
- (51) Yang, Y.; Liu, Z.; Chen, J.; Cai, Z.; Wang, Z.; Chen, W.; Zhang, G.; Zhang, X.; Chi, L.; Zhang, D. A Facile Approach to Improve Interchain Packing Order and Charge Mobilities by Self-Assembly of Conjugated Polymers on Water. *Adv. Sci.* **2018**, *5*, No. 1801497.
- (52) Song, X.; Gasparini, N.; Ye, L.; Yao, H.; Hou, J.; Ade, H.; Baran, D. Controlling Blend Morphology for Ultrahigh Current Density in Nonfullerene Acceptor-Based Organic Solar Cells. *ACS Energy Lett.* **2018**, *3*, 669–676.
- (53) Chang, Y.; Zhang, X.; Tang, Y.; Gupta, M.; Su, D.; Liang, J.; Yan, D.; Li, K.; Guo, X.; Ma, W.; Yan, H.; Zhan, C. 14%-Efficiency Fullerene-Free Ternary Solar Cell Enabled by Designing a Short Side-Chain Substituted Small-Molecule Acceptor. *Nano Energy* **2019**, *64*, No. 103934.
- (\$4) Zhao, H.; Zhang, L.; Naveed, H. B.; Lin, B.; Zhao, B.; Zhou, K.; Gao, C.; Zhang, C.; Wang, C.; Ma, W. Processing-Friendly Slot-Die-Cast Nonfullerene Organic Solar Cells with Optimized Morphology. ACS Appl. Mater. Interfaces 2019, 11, 42392–42402.
- (55) Verploegen, E.; Miller, C. E.; Schmidt, K.; Bao, Z.; Toney, M. F. Manipulating the Morphology of P3HT-PCBM Bulk Heterojunction Blends with Solvent Vapor Annealing. *Chem. Mater.* **2012**, 24, 3923–3931.
- (56) Taliani, C.; Ruani, G.; Zamboni, R.; Danieli, R.; Rossini, S.; Denisov, V. N.; Burlakov, V. M.; Negri, F.; Orlandi, G.; Zerbetto, F. Light-Induced Oxygen Incision of C60. *J. Chem. Soc., Chem. Commun.* 1993, 3, 220.
- (57) Heumueller, T.; Mateker, W. R.; Distler, A.; Fritze, U. F.; Cheacharoen, R.; Nguyen, W. H.; Biele, M.; Salvador, M.; von Delius, M.; Egelhaaf, H.-J.; McGehee, M. D.; Brabec, C. J. Morphological and Electrical Control of Fullerene Dimerization Determines Organic Photovoltaic Stability. *Energy Environ. Sci.* **2016**, *9*, 247–256.
- (58) Distler, A.; Sauermann, T.; Egelhaaf, H.-J.; Rodman, S.; Waller, D.; Cheon, K.-S.; Lee, M.; Guldi, D. M. The Effect of PCBM Dimerization on the Performance of Bulk Heterojunction Solar Cells. *Adv. Energy Mater.* **2014**, *4*, No. 1300693.
- (59) Kim, T.; Younts, R.; Lee, W.; Lee, S.; Gundogdu, K.; Kim, B. J. Impact of the Photo-Induced Degradation of Electron Acceptors on the Photophysics, Charge Transport and Device Performance of All-Polymer and Fullerene—Polymer Solar Cells. *J. Mater. Chem. A* **2017**, 5, 22170—22179.
- (60) Zhu, Y.; Gadisa, A.; Peng, Z.; Ghasemi, M.; Ye, L.; Xu, Z.; Zhao, S.; Ade, H. Rational Strategy to Stabilize an Unstable High-Efficiency Binary Nonfullerene Organic Solar Cells with a Third Component. *Adv. Energy Mater.* **2019**, *9*, No. 1900376.
- (61) Liu, F.; Ferdous, S.; Schaible, E.; Hexemer, A.; Church, M.; Ding, X.; Wang, C.; Russell, T. P. Fast Printing and In Situ

Pursuant to the DOE Public Access Plan, this document represents the authors' peer-reviewed, accepted manuscript.

The published version of the article is available from the relevant publisher.

ACS Applied Materials & Interfaces

www.acsami.org

Research Article

Morphology Observation of Organic Photovoltaics Using Slot-Die Coating. Adv. Mater. 2015, 27, 886–891.

- (62) Richter, L. J.; DeLongchamp, D. M.; Amassian, A. Morphology Development in Solution-Processed Functional Organic Blend Films: An In Situ Viewpoint. *Chem. Rev.* **2017**, *117*, 6332–6366.
- (63) Oosterhout, S. D.; Savikhin, V.; Zhang, J.; Zhang, Y.; Burgers, M. A.; Marder, S. R.; Bazan, G. C.; Toney, M. F. Mixing Behavior in Small Molecule:Fullerene Organic Photovoltaics. *Chem. Mater.* **2017**, 29, 3062–3069.
- (64) Beaucage, G. Combined Small-Angle Scattering for Characterization of Hierarchically Structured Polymer Systems over Nano-to-Micron Meter. In *Polymer Science: A Comprehensive Reference*; Elsevier, 2012; pp 399–409.